Graphene Quantum Strain Transistors

A. C. McRae, G. Wei, and A. R. Champagne*
Department of Physics, Concordia University, Montreal, Quebec, H4B 1R6, Canada
*E-mail: a.champagne@concordia.ca

Supplemental Material

S1. Electrostatic and thermal strain in the proposed GQST devices

1.1 Thermal strain in suspended graphene devices

The total thermal strain in the graphene channel, $\varepsilon_{\text{thermal}} = (\Delta L)_{\text{thermal}}/L$, is determined by three contributions, the thermal strain from substrate contraction $\varepsilon_{\text{th,sub}}$, the thermal strain from gold contraction $\varepsilon_{\text{th,Au}}$, and the thermal strain from expansion of the graphene flake $\varepsilon_{\text{th,g}}$, as the device is cooled. These are illustrated in Fig. S1(a).

Based on our device geometry, $\varepsilon_{\text{th,sub}}$ is given by the thermal strain in the Si substrate. As the chip is cooled, the Si contracts and compresses the graphene channel [S1]. The two suspended gold beams are deposited on a SiO_2 layer, and they clamp the suspended graphene. The gold cantilevers contract as they are cooled, applying strain to the graphene channel [S2]. Graphene itself has a negative thermal expansion coefficient [S3]. From Fig. S1(a), we see that the direction of the thermal expansion of the graphene is aligned with the contraction of the gold beams. Because the gold beams' thermal displacements are much larger than the graphene channel's thermal expansion, the stretching of the channel is determined, at low temperature, by the gold thermal expansion. The total thermal strain $\varepsilon_{\text{thermal}}$ in the channel is given by Eq. S1.

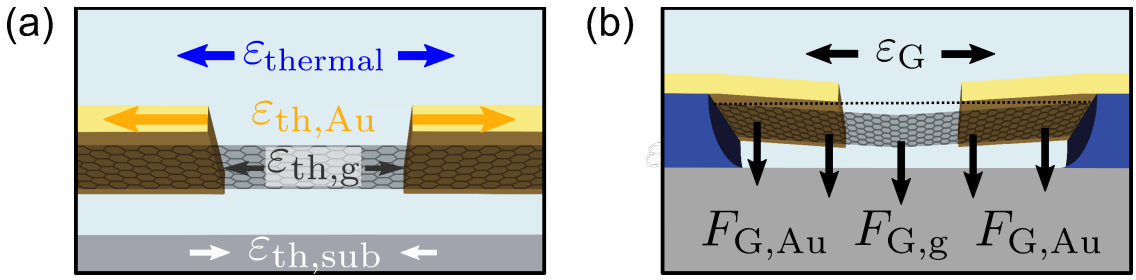

Figure S1. Electrostatic and thermal strains in suspended graphene devices. (a) Thermal strains as temperature decreases: contraction of the Au film and substrate, and expansion of the graphene channel. (b) Electrostatic strain from the attractive force between the back gate and the graphene.

$$\varepsilon_{\text{thermal}} = \int_{300}^{T} \alpha_{\text{Si}}(t)dt - \frac{u-L}{L}\int_{300}^{T} \alpha_{\text{Au}}(t)dt, \tag{S1a}$$

$$\varepsilon_{\text{th,g}} = \int_{300}^{T} \alpha_{\text{g}}(t)dt, \tag{S1b}$$

with α_{Si}, α_{Au}, and α_{g} the coefficients of thermal expansion for silicon, gold, and graphene respectively, $u = 900$ nm is the undercut length, and $L = 100$ nm is the length of the suspended graphene channel. Calculating the individual contributions to strain at $T = 1$ K gives $\varepsilon_{\text{th,sub}} \approx -0.04$ % [S1], $\varepsilon_{\text{th,Au}} \approx 2.6$ % [S2], and $\varepsilon_{\text{th,g}} \approx -0.2$ % [S3]. The total thermal strain in the channel is $\varepsilon_{\text{thermal}} = \varepsilon_{\text{th,sub}} + \varepsilon_{\text{th,Au}} \approx 2.6$ %.

1.2 Electrostatic strain in a suspended graphene device

An electrostatic strain, ε_{G}, of the channel arises from the pull of V_{G}, as shown in Fig. S1 (b). There are two separate sources of ε_{G}: an electrostatic pull on the graphene channel $\varepsilon_{\text{G,g}}$, and one on the suspended gold cantilevers $\varepsilon_{\text{G,Au}}$. We first mention that given the modest $V_{\text{G}} \leq 10$ V needed in experiments, and the thickness of gold beams (120 nm), the electrostatic deflection of the beams is completely negligible [S4], thus $\varepsilon_{\text{G,Au}} = 0$ %. The strain caused by the gating force directly on the channel is given by [S5]:

$$\varepsilon_{\text{G,g}} = P\frac{L^2}{8Y_{\text{2D}}h_0}, \tag{S2}$$

where $P = F_{\text{G,g}}/LW = (C_{\text{G}}V_{\text{G}})^2/2\epsilon_0$ is the electrostatic pressure on the graphene channel, $F_{\text{G,g}}$ is the electrostatic force, $Y_{\text{2D}} \approx 340$ N/m is the 2D Young's modulus of graphene, ϵ_0 is the vacuum permittivity, and h_0 is the maximum deflection for a parabolic deformation of the graphene flake. The value of h_0 is calculated from [S5]:

$$\left(h_0^2 - \frac{3}{16}L\Delta L\right)h_0 = \frac{3}{128}\frac{PL^4}{Y_{\text{2D}}}, \tag{S3}$$

where ΔL is the built-in stretch (see section 1.1) of the suspended channel, and is positive (negative) for tension (compression). The resulting $\varepsilon_{\text{G,g}}$ is plotted versus V_{G} in Fig. 1(c) of the main text, and is typically $\sim$0.01 %. It is negligible compared to both the thermal and mechanically controlled strains, and we exclude it from our calculations.

S2. Uniaxially-strained graphene: band structure and ballistic transmission

2.1 Transmission in unstrained ballistic graphene

We start with the ballistic transmission in unstrained graphene as a reference point [S6]:

$$T_n = \left| \frac{k_x \tilde{k}_x}{k_x \tilde{k}_x \cos[\tilde{k}_x L] - i\left(k_F \tilde{k}_F - q_n^2\right)\sin[\tilde{k}_x L]} \right|^2, \tag{S4}$$

where $q_n = \pi/W\,(n+1/2)$ is the transversal momentum, $k_F = \Delta\mu_{\text{contact}}/\hbar v_F$, and $k_x = (k_F^2 - q_n^2)^{1/2}$ are respectively the total and longitudinal (x-axis) momenta in the contacts, while $\tilde{k}_F = \Delta\mu_{\text{G}}/\hbar v_F$ and $\tilde{k}_x = \left(\tilde{k}_F^2 - \tilde{q}_n^2\right)^{1/2}$ are respectively the total and longitudinal momenta in the channel, $v_F = 8.8 \times 10^5$ m/s, and $\tilde{q}_n = q_n$, due to transversal momentum conservation across the contact/channel boundary. As in the main text, $\Delta\mu_{\text{contact}}$ is the contact doping, while the doping in the channel induced by the back gate is $\Delta\mu_{\text{G}} = \text{sgn}(V_{\text{G}} - V_{\text{D}})\hbar v_F\sqrt{\pi(V_{\text{G}} - V_{\text{D}})C_{\text{G}}/e}$. The conductivity is then [S6]:

$$\sigma = \frac{L}{W}\frac{4e^2}{h}\sum_{n=0}^{N} T_n, \tag{S5}$$

where $N = \text{Int}(k_F W/\pi - 1/2)$ is the number of allowed modes set by the Fermi energy in the graphene contacts. We set $L = 100$ nm, $W = 1000$ nm, and $C_{\text{G}} = 1.7 \times 10^{-8}$ F/cm^2 (as in the main text). In Fig. S2, we plot $\sigma - V_{\text{G}}$ data as a function of $\Delta\mu_{\text{contact}}$ ranging from -0.2 to 0.2 eV, as well as for the infinite limit. When $\Delta\mu_{\text{contact}} \gg \Delta\mu_{\text{G}}$, the allowed carrier trajectories are nearly normally incident on the channel, resulting in symmetric behavior for electrons and holes. When $\Delta\mu_{\text{contact}} \sim \Delta\mu_{\text{G}}$ a significant electron-hole conductivity asymmetry arises. We define the relative asymmetry as $\eta = 2(\sigma_h - \sigma_e)/(\sigma_h + \sigma_e)$, as in the main text, Fig. 3(c) and (f). The sign of the asymmetry depends on the sign of the contact doping, as seen by comparing the solid and dashed data in Fig. S2. The conductivity minimum is $\sigma = 4e^2/\pi h$, as expected for ballistic graphene with $W/L \gg 1$.

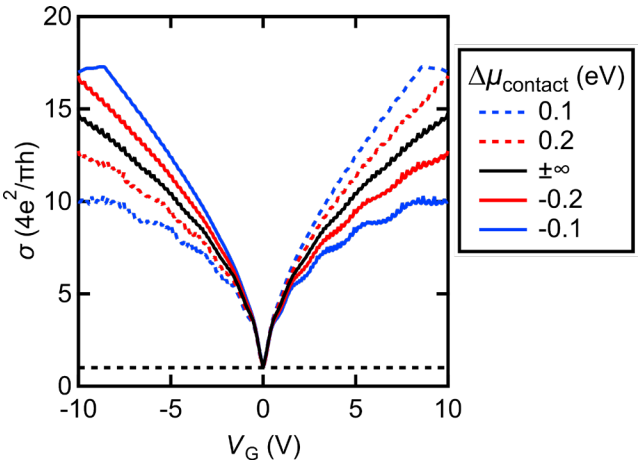

Figure S2. $\sigma - V_{\text{G}}$ in unstrained graphene for various $\Delta\mu_{\text{contact}}$. The device dimensions are $L = 100$ nm, and $W = 1000$ nm. For large contact doping, there is no transport asymmetry, while for small contact doping, the sign of the asymmetry depends on the sign of the contact doping.

2.2 Tight-binding parameter values

In Table S1 we list the tight-binding parameter values used in our calculations.

Parameter	a	γ_0	ν	β	g_ε
Value	1.42 Å [S7]	-2.7 eV [S7]	0.165 [S8]	2.5 [S8]	3.0 eV [S9]

Table S1. Tight-binding parameter values used in our calculations: a, the nearest neighbor distance, γ_0, the nearest neighbor hopping parameter, ν, the Poisson ratio, β, the electronic Grüneisen parameter, and g_ε, the strain-induced scalar potential magnitude.

The nearest neighbor spacing ($a = 1.42$ Å) and hopping parameter ($\gamma_0 = -2.7$ eV) are well established in literature [S7]. The Poisson ratio, ν, of graphene is most often cited as having the value 0.165, based on measurements of the basal plane of graphite [S8]. The unitless electronic Grüneisen parameter ($\beta = -d\ln[\gamma_0]/\,d\ln[a]$) can be measured via Raman spectroscopy and has been reported to range from 2 to 3.37 [S8, S10]. In our model we use $\beta = 2.5$, which is roughly the average reported value. The calculated magnitude of the strain-induced scalar potential (self-doping) in graphene has been reported over a range, $\Delta\mu_\varepsilon = g_\varepsilon(1-\nu)\,\varepsilon_{\text{total}} = 1.7$ eV - 3.75 eV $\times\ \varepsilon_{\text{total}}$. We choose a value often cited in literature, from *ab. initio* calculations, $g_\varepsilon = 3.0$ eV [S9].

2.3 Tight-binding band structure of strained graphene

The real space lattice of graphene, with its zig-zag direction along the x-axis ($\theta = 0°$), is shown in Fig. S3(a). The nearest-neighbor vectors are [S8]:

$$\boldsymbol{\delta}_1 = \frac{a}{2}\mathcal{R}(\theta)\cdot\left(\sqrt{3},1\right), \qquad \boldsymbol{\delta}_2 = \frac{a}{2}\mathcal{R}(\theta)\cdot\left(-\sqrt{3},1\right), \qquad \boldsymbol{\delta}_3 = a\,\mathcal{R}(\theta)\cdot(0,-1), \tag{S6}$$

where the rotation matrix $\mathcal{R}(\theta)$ accounts for an arbitrary crystal orientation:

$$\mathcal{R}(\theta) = \begin{pmatrix}\cos\theta & -\sin\theta \\ \sin\theta & \cos\theta\end{pmatrix}. \tag{S7}$$

The lattice's primitive vectors are:

$$\boldsymbol{a}_1 = \frac{a}{2}\mathcal{R}(\theta)\cdot\left(\sqrt{3},3\right), \qquad \boldsymbol{a}_2 = \frac{a}{2}\mathcal{R}(\theta)\cdot\left(-\sqrt{3},3\right). \tag{S8}$$

And the corresponding reciprocal lattice vectors, shown in Fig. S3(b), are:

$$\boldsymbol{b}_1 = \frac{2\pi}{3a}\mathcal{R}(\theta)\cdot\left(\sqrt{3},1\right), \qquad \boldsymbol{b}_2 = \frac{2\pi}{3a}\mathcal{R}(\theta)\cdot\left(-\sqrt{3},1\right), \tag{S9}$$

The $\boldsymbol{b}_{1,2}$ define the first Brillouin Zone (FBZ), whose corners are the $\boldsymbol{K}_i$ points:

$$\boldsymbol{K}_1 = \frac{4\pi}{3\sqrt{3}a}\mathcal{R}(\theta)\cdot(1,0), \qquad \boldsymbol{K}_2 = \frac{4\pi}{3\sqrt{3}a}\mathcal{R}(\theta)\cdot\left(-\frac{1}{2},\frac{\sqrt{3}}{2}\right), \qquad \boldsymbol{K}_3 = \frac{4\pi}{3\sqrt{3}a}\mathcal{R}(\theta)\cdot\left(-\frac{1}{2},-\frac{\sqrt{3}}{2}\right), \tag{S10}$$

and $\boldsymbol{K}_i' = -\boldsymbol{K}_i$.

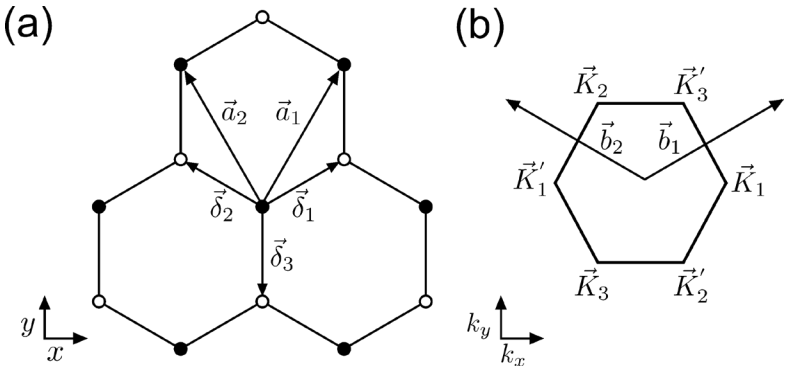

Figure S3. (a) Real space graphene lattice with the zig-zag direction aligned along the x-axis ($\theta = 0°$), showing nearest neighbor vectors $\boldsymbol{\delta}_n$, and primitive vectors $\boldsymbol{a}_1, \boldsymbol{a}_2$. Sublattice A (filled circles) and sublattice B (open circles) are shown. (b) First Brillouin zone (FBZ) of graphene corresponding to (a), showing the reciprocal lattice vectors $\boldsymbol{b}_1, \boldsymbol{b}_2$, and $K_i^{(\prime)}$ points.

The momentum-space tight-binding Hamiltonian, considering nearest neighbor (nn) hopping, γ_0, and next-nearest neighbor (nnn) hopping, γ_0', is [S7,S8]:

$$H_0 = \gamma_0 \sum_{\boldsymbol{k},n} (e^{-i\boldsymbol{k}\cdot\boldsymbol{\delta}_n} a_{\boldsymbol{k}}^\dagger b_{\boldsymbol{k}} + \text{H.c.}) + \gamma_0' \sum_{\boldsymbol{k},n\neq m} (\, e^{-i\boldsymbol{k}\cdot(\boldsymbol{\delta}_n - \boldsymbol{\delta}_m)} (a_{\boldsymbol{k}}^\dagger a_{\boldsymbol{k}} + b_{\boldsymbol{k}}^\dagger b_{\boldsymbol{k}}) + \text{H.c.}), \quad \text{(S11)}$$

where $a_{\boldsymbol{k}}^\dagger$ ($a_{\boldsymbol{k}}$) creates (destroys) an electron on sublattice A, and $b_{\boldsymbol{k}}^\dagger$ ($b_{\boldsymbol{k}}$) do the same on sublattice B. The electronic energy dispersion is then given by:

$$E_0 = \pm\left|\textstyle\sum_n \gamma_0 e^{-i\boldsymbol{k}\cdot\boldsymbol{\delta}_n}\right| = \pm\gamma_0\sqrt{3 + f(\boldsymbol{k})} + \gamma_0' f(\boldsymbol{k}), \quad \text{(S12)}$$

where

$$f(\boldsymbol{k}) = 2\cos\left(\sqrt{3}k_x a\right) + 4\cos\left(\frac{\sqrt{3}}{2}\, k_x a\right)\cos\left(\frac{3}{2}k_y a\right). \quad \text{(S13)}$$

We can expand Eq. S13 to derive the low energy dispersion around $\boldsymbol{k} = \boldsymbol{K}$ when $(\boldsymbol{k} - \boldsymbol{K}) \ll \boldsymbol{K}$**.** For this low energy expansion, the nnn term in Eq. S12 is nearly constant, and results in a rigid shift of the low energy dispersion [S7].

When strain is applied, the real and reciprocal vectors are modified to first order in strain as [S8]:

$$\boldsymbol{a}_i \to (\bar{\boldsymbol{I}} + \bar{\boldsymbol{\varepsilon}}) \cdot \boldsymbol{a}_i, \qquad \boldsymbol{b}_i \to (\bar{\boldsymbol{I}} - \bar{\boldsymbol{\varepsilon}}) \cdot \boldsymbol{b}_i, \quad \text{(S14)}$$

where $\bar{\boldsymbol{I}}$ is the identity matrix, $\bar{\boldsymbol{\varepsilon}}$ is the strain tensor, and $i = 1,2$. For uniaxial strain in x:

$$\bar{\boldsymbol{\varepsilon}} = \begin{pmatrix} \varepsilon_{xx} & \varepsilon_{xy} \\ \varepsilon_{yx} & \varepsilon_{yy} \end{pmatrix} = \begin{pmatrix} \varepsilon & 0 \\ 0 & -\nu\varepsilon \end{pmatrix}, \quad \text{(S15)}$$

where ν is the Poisson ratio. Focusing only on the nn term, the strained Hamiltonian is

$$H = \sum_{\boldsymbol{k},n} (\gamma_n e^{-i\boldsymbol{k}\cdot(\bar{\boldsymbol{I}}+\bar{\boldsymbol{\varepsilon}})\cdot\boldsymbol{\delta}_n} a_{\boldsymbol{k}}^\dagger b_{\boldsymbol{k}} + \text{H.c.}), \quad \text{(S16)}$$

with the strain-modified hopping parameter:

$$\gamma_n = \gamma_0 \exp[-\beta\{|(\bar{\boldsymbol{I}} + \bar{\boldsymbol{\varepsilon}}) \cdot \boldsymbol{\delta}_n|/a - 1\}], \tag{S17}$$

This gives the dispersion [S8]:

$$E = \pm \left| \sum_n \gamma_n e^{-i\boldsymbol{k}\cdot(\bar{\boldsymbol{I}}+\bar{\boldsymbol{\varepsilon}})\cdot\boldsymbol{\delta}_n} \right| = \pm\sqrt{\gamma + g(\boldsymbol{k})}, \tag{S18}$$

where $\gamma = \gamma_1^2 + \gamma_2^2 + \gamma_3^2$, and

$$g(\boldsymbol{k}) = \sum_{n=1}^{3} \sum_{m>n}^{3} 2\gamma_n\gamma_m \cos[\boldsymbol{k} \cdot (\bar{\boldsymbol{I}} + \bar{\boldsymbol{\varepsilon}}) \cdot (\boldsymbol{\delta}_n - \boldsymbol{\delta}_m)]. \tag{S19}$$

For small strains, we can expand Eq. S16 to first order in strain [S11]:

$$H = \sum_{\boldsymbol{k},n} (\gamma_0 - \gamma_0 \frac{\beta}{a^2} \boldsymbol{\delta}_n \cdot \bar{\boldsymbol{\varepsilon}} \cdot \boldsymbol{\delta}_n - i\gamma_0 \boldsymbol{k} \cdot \bar{\boldsymbol{\varepsilon}} \cdot \boldsymbol{\delta}_n) e^{-i\boldsymbol{k}\cdot\boldsymbol{\delta}_n} \, (a_{\boldsymbol{k}}^{\dagger} b_{\boldsymbol{k}} + \text{H.c.}). \tag{S20}$$

From Eq. S20, we can identify the two distinct changes to the Hamiltonian arising from strain. The second term in Eq. S20 is from the strain modification of the electron hopping amplitude, as per Eq. S17. The third term in Eq. S20 is from the stretching of the nn distances, as per Eq. S16. These two terms will translate into the two types of strain-induced vector potentials in the Dirac notation of the Hamiltonian.

2.4 Dirac Hamiltonian and vector potentials in uniaxially-strained graphene

We can express the tight-binding Hamiltonian from Eq. S20 in a Dirac form [S8], as shown in Eq. S21:

$$H_{K_i} = \hbar v_F (\bar{\boldsymbol{I}} + (1-\beta)\bar{\boldsymbol{\varepsilon}}) \cdot \boldsymbol{\sigma} \cdot \left(\tilde{\boldsymbol{k}} - \boldsymbol{A}_i\right) + \Delta\mu_{\text{G}} + \Delta\mu_{\varepsilon}. \tag{S21}$$

This Hamiltonian describes the three K_i valleys, and can be modified to describe the three K_i' valleys by changing the sign of $\boldsymbol{A}_i$. The $\boldsymbol{\sigma}$ are the Pauli spin matrices, and $\Delta\mu_{\text{G}}$ is the potential from electrostatic gating. The strain-induced scalar potential [S7, S10] is given by $\Delta\mu_{\varepsilon} = g_{\varepsilon}(\varepsilon_{xx} + \varepsilon_{yy})$, where g_{ε} depends on the change of the nnn hopping with strain. For uniaxial strain, the scalar potential is $\Delta\mu_{\varepsilon} = g_{\varepsilon}(1-\nu)\varepsilon$. The strain-induced vector gauge potentials, $\boldsymbol{A}_i$, depend on the modification of both the nn hoppings and nn distances. From expanding about the strained Dirac points [S8], we find the anisotropic Fermi velocity tensor $\bar{\boldsymbol{v}}_F = v_F(\bar{\boldsymbol{I}} + (1-\beta)\bar{\boldsymbol{\varepsilon}})$, with matrix elements $v_{F,xx} = v_F(1 + (1-\beta)\varepsilon)$ and $v_{F,yy} = v_F(1 - (1-\beta)\nu\varepsilon)$ for uniaxial strain.

The vector potentials are defined by the shift in the momenta of the Dirac points in reciprocal space as shown in Fig. S4. The locations of the Dirac points under stain are $\boldsymbol{K}_{D,i} = \boldsymbol{K}_i + \boldsymbol{A}_i$, where the $\boldsymbol{K}_i$ are the corners of the unstrained FBZ. We show below how the vector potentials are calculated.

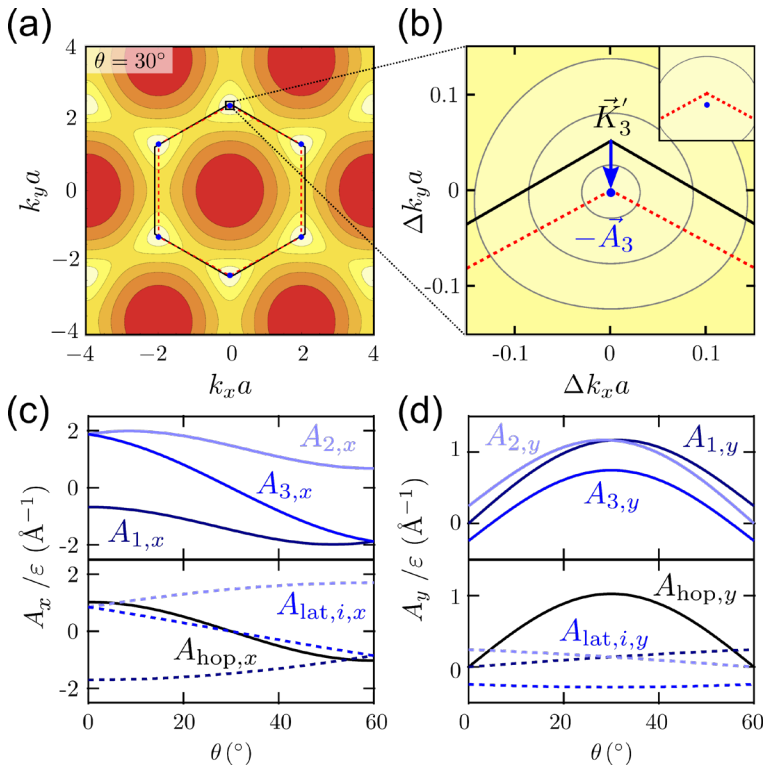

Figure S4. Vector potentials in uniaxially strained graphene. Contour plot of the graphene band structure for $\varepsilon_{\mathrm{total}} = 5.1\ \%$ at $\theta = 30°$. We show the unstrained FBZ (black), the strained FBZ (red, dashed), and strained Dirac points (blue dots). (b) Zoom-in on one FBZ corner. The inset in is a further zoom-in of the same data, showing that the new Dirac point does not lie at the corner of the strained FBZ. (c) - (d) The top plots show the x and y components of the $\boldsymbol{A}_i$ as a function of θ. The bottom plots show the two terms, $\boldsymbol{A}_{\mathrm{hop}}$ (solid black) and $\boldsymbol{A}_{\mathrm{lat,i}}$ (dashed blue) which make up the $\boldsymbol{A}_i$.

In Fig. S4(a), we show contour plots of the dispersion for graphene with $\varepsilon = 5.1\ \%$ at $\theta = 30°$, as calculated using Eq. S20, showing the unstrained FBZ (black lines), strained FBZ (red dashed lines), and the Dirac point positions (blue dots). In Fig. S4(b), we show a zoom-in on one of the Dirac points from panel (a). Here we see the position of the strained Dirac point and FBZ, relative to the unstrained FBZ. The inset shows a further zoomed-in view, where we see that the Dirac point does not lie at the corner of the strained FBZ.

It follows from Eq. S20 that the vector potentials have the form [S8, S11],

$$\boldsymbol{A}_i = -\bar{\boldsymbol{\varepsilon}} \cdot \boldsymbol{K}_i + \boldsymbol{A}_{\mathrm{hop}}, \qquad \boldsymbol{A}_{\mathrm{hop}} = \frac{\beta}{2a}\begin{pmatrix} \varepsilon_{xx} - \varepsilon_{yy} \\ -2\varepsilon_{xy} \end{pmatrix}. \tag{S22}$$

To generalize this formula for any θ, we rotate $\bar{\boldsymbol{\varepsilon}}$ in the lattice frame [S12]:

$$\bar{\boldsymbol{\varepsilon}}' = \mathcal{R}^{-1}(\theta) \cdot \bar{\boldsymbol{\varepsilon}} \cdot \mathcal{R}(\theta) = \varepsilon \begin{pmatrix} \cos^2\theta - \nu \sin^2\theta & -(1+\nu)\cos\theta \sin\theta \\ -(1+\nu)\cos\theta \sin\theta & -\nu\cos^2\theta + \sin^2\theta \end{pmatrix}. \tag{S23}$$

The vector potentials in the lattice frame are then,

$$\boldsymbol{A}_1' = \frac{4\pi}{3\sqrt{3}a}\varepsilon \begin{pmatrix} -\cos^2\theta + \nu\sin^2\theta \\ (1+\nu)\cos\theta\sin\theta \end{pmatrix} + \boldsymbol{A}_{\mathrm{hop}}' \tag{S24a}$$

$$\boldsymbol{A}_2' = \frac{2\pi}{3a}\varepsilon\begin{pmatrix} \frac{1}{\sqrt{3}}(\cos^2\theta - \nu\sin^2\theta) + (1+\nu)\cos\theta\sin\theta \\ -(-\nu\cos^2\theta + \sin^2\theta) - \frac{1}{\sqrt{3}}(1+\nu)\cos\theta\sin\theta \end{pmatrix} + \boldsymbol{A}_{\text{hop}}', \tag{S24b}$$

$$\boldsymbol{A}_3' = \frac{2\pi}{3a}\varepsilon\begin{pmatrix} \frac{1}{\sqrt{3}}(\cos^2\theta - \nu\sin^2\theta) - (1+\nu)\cos\theta\sin\theta \\ (-\nu\cos^2\theta + \sin^2\theta) - \frac{1}{\sqrt{3}}(1+\nu)\cos\theta\sin\theta \end{pmatrix} + \boldsymbol{A}_{\text{hop}}', \tag{S24c}$$

$$\boldsymbol{A}_{\text{hop}}' = \frac{\beta}{2a}\varepsilon(1+\nu)\begin{pmatrix}\cos 2\theta \\ \sin 2\theta\end{pmatrix}. \tag{S24d}$$

In the lattice frame, the Hamiltonian is:

$$(H_{\boldsymbol{K}_i})' = \hbar v_F(\bar{\boldsymbol{I}} + (1-\beta)\bar{\boldsymbol{\varepsilon}}')\cdot\boldsymbol{\sigma}\cdot\left(\tilde{\boldsymbol{k}}' - \boldsymbol{A}_i'\right) + \Delta\mu_{\text{G}} + \Delta\mu_{\varepsilon}, \tag{S25}$$

Since we are interested in calculating $\boldsymbol{A}_i$ in the lab frame, we rotate $(H_{\boldsymbol{K}_i})'$ back into the lab frame using the unitary matrix for rotating a spinor [S10]:

$$U^{\dagger}(\theta) = \begin{pmatrix}1 & 0 \\ 0 & e^{i\theta}\end{pmatrix}. \tag{S26}$$

Then $H = U^{\dagger}(-\theta)H'U(-\theta)$. This gives the vector potentials in the lab frame reported in Eq. 2 of the main text:

$$\boldsymbol{A}_1 = \frac{4\pi\varepsilon}{3\sqrt{3}a}\begin{pmatrix}-\cos\theta \\ \nu\sin\theta\end{pmatrix} + \boldsymbol{A}_{\text{hop}}, \tag{S27a}$$

$$\boldsymbol{A}_2 = \frac{2\pi\varepsilon}{3a}\begin{pmatrix} \frac{1}{\sqrt{3}}\cos\theta + \sin\theta \\ -\frac{1}{\sqrt{3}}\nu\sin\theta + \nu\cos\theta \end{pmatrix} + \boldsymbol{A}_{\text{hop,}} \tag{S27b}$$

$$\boldsymbol{A}_3 = \frac{2\pi\varepsilon}{3a}\begin{pmatrix} \frac{1}{\sqrt{3}}\cos\theta - \sin\theta \\ -\frac{1}{\sqrt{3}}\nu\sin\theta - \nu\cos\theta \end{pmatrix} + \boldsymbol{A}_{\text{hop,}}, \tag{S27c}$$

$$\boldsymbol{A}_{\text{hop}} = \frac{\beta\varepsilon(1+\nu)}{2a}\begin{pmatrix}\cos 3\theta \\ \sin 3\theta\end{pmatrix}. \tag{S27d}$$

The x and y components of the vector potentials are plotted as a function θ in Fig. S4(c) and S4(d) respectively. In the top plots, we show the total vector potentials from Eq. S27, while in the bottom plots we show the hopping and lattice contributions.

2.4 Transmission across uniaxial-strain barriers in graphene

To derive the transmission equation in uniaxially strained graphene devices, we use the Hamiltonian operator in Eq. S21. We solve for the wave functions of carriers in strained graphene using the Hamiltonian:

$$H_{\boldsymbol{K}_i}\,\boldsymbol{\Psi}_{i,n,k_x} = \begin{pmatrix} \Delta\mu_{\mathrm{G}} + \Delta\mu_{\varepsilon} & \hbar v_{F,xx}\left(k_x - A_{i,x}\right) - i\hbar v_{F,yy}(q_n - A_{i,y}) \\ \hbar v_{F,xx}\left(k_x - A_{i,x}\right) + i\hbar v_{F,yy}(q_n - A_{i,y}) & \Delta\mu_{\mathrm{G}} + \Delta\mu_{\varepsilon} \end{pmatrix} \boldsymbol{\Psi}_{i,n,k_x}. \tag{S28}$$

We diagonalize the Hamiltonian to determine the wave functions [S6]:

$$\boldsymbol{\Psi}_{i,n,k_x} = e^{ik_x x}\chi_{i,n,k_x} \tag{S29}$$

with

$$\chi_{i,n,k_x} = a_{i,n}e^{iq_n y}\begin{pmatrix}1\\ z_{i,n,k_x}\end{pmatrix} + b_{i,n}e^{-iq_n y}\begin{pmatrix}z_{i,n,k_x}\\ 1\end{pmatrix}, \tag{S30}$$

and

$$z_{i,n,k_x} = \pm\frac{v_{F,xx}(k_x - A_{i,x}) + iv_{F,yy}(q_n - A_{i,y})}{\sqrt{v_{F,xx}^2(k_x - A_{i,x})^2 + v_{F,yy}^2(q_n - A_{i,y})^2}}. \tag{S31}$$

where the $\pm$ refers to the conduction and valence bands respectively. We then make use of the x-boundary conditions illustrated in Fig. S5.

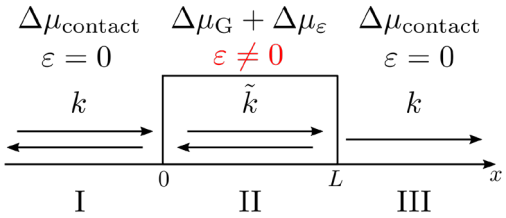

Figure S5. Boundary condition along x in a suspended graphene device. Regions I and III are the graphene contacts covered by gold, and region II is the naked and strained channel.

We label the charge carrier momenta in the contacts and channel, respectively $\boldsymbol{k} = k_x\hat{x} + q_n\hat{y}$ and $\tilde{\boldsymbol{k}} = \tilde{k}_x\hat{x} + \tilde{q}_n\hat{y}$. Then, the wave function in the three regions shown in Fig. S5 is:

$$\boldsymbol{\Psi}_{\mathrm{I}} = \chi_{i,n,k_x}e^{ik_x x} + r_{i,n}\chi_{i,n,-k_x}e^{-ik_x x}, \tag{S32a}$$
$$\boldsymbol{\Psi}_{\mathrm{II}} = \alpha_{i,n}\chi_{i,n,\tilde{k}_x}e^{i\tilde{k}_x x} + \beta_{i,n}\chi_{i,n,-\tilde{k}_x}e^{-i\tilde{k}_x x}, \tag{S32b}$$
$$\boldsymbol{\Psi}_{\mathrm{III}} = t_{i,n}\chi_{i,nk_x}e^{ik_x(x-L)}. \tag{S32c}$$

Setting $\Psi_{\mathrm{I}} = \Psi_{\mathrm{II}}$ and $\Psi_{\mathrm{II}} = \Psi_{\mathrm{III}}$ at the boundaries $x = 0$ and $x = L$ give the system of equations:

$$\begin{pmatrix}1\\ z_{i,n,k_x}\end{pmatrix} + r_{i,n}\begin{pmatrix}1\\ z_{i,n,-k_x}\end{pmatrix} = \alpha_{i,n}\begin{pmatrix}1\\ z_{i,n,\tilde{k}_x}\end{pmatrix} + \beta_{i,n}\begin{pmatrix}1\\ z_{i,n,-\tilde{k}_x}\end{pmatrix}, \tag{S33a}$$
$$t_{i,n}\begin{pmatrix}1\\ z_{i,n,k_x}\end{pmatrix} = \alpha_{i,n}\begin{pmatrix}1\\ z_{i,n,\tilde{k}_x}\end{pmatrix}e^{i\tilde{k}_x L} + \beta_{i,n}\begin{pmatrix}1\\ z_{i,n,-\tilde{k}_x}\end{pmatrix}e^{-i\tilde{k}_x L}, \tag{S33b}$$

which we solve for the transmission, $T_{\xi,i,n} = \left|t_{\xi,i,n}\right|^2$. We find:

$$T_{\xi,i,n} = \frac{\left(\frac{v_{F,xx}}{v_F} k_x \tilde{k}_x\right)^2}{\left(\frac{v_{F,xx}}{v_F} k_x \tilde{k}_x\right)^2 \cos^2\left[\tilde{k}_x L\right] + \left[k_F \tilde{k}_F - \frac{v_{F,yy}}{v_F} q_n\left(q_n - \xi A_{i,y}\right)\right]^2 \sin^2\left[\tilde{k}_x L\right]}, \quad \text{(S34)}$$

where $\xi = \pm 1$ refers to the K and K' valleys respectively, $q_n = \pi/W\ (n + 1/2)$ is the quantized transversal momentum for mode n using smooth edge boundary conditions [S6], and $k_x = (k_F^2 - q_n^2)^{1/2}$, $\tilde{k}_x = v_{F,xx}^{-1}[v_F^2 \tilde{k}_F^2 - v_{F,yy}^2\left(q_n - A_{i,y}\right)^2]^{\frac{1}{2}}$. The number of available modes is set by the contact potential,

$$N = \mathrm{Int}\left(\frac{W}{\pi} * k_F - \frac{1}{2}\right). \quad \text{(S35)}$$

Summing over these modes gives the ballistic conductivity:

$$\sigma = \frac{L}{W} \frac{2e^2}{h} \frac{1}{3} \sum_{\xi} \sum_{i}^{3} \sum_{n}^{N} T_{\xi,i,n}. \quad \text{(S36)}$$

S3. Hierarchy of the sources of uncertainty in GQST calculations

We present the hierarchy of sources of uncertainty in the model. We begin by discussing the main additions we made to previous idealized model, parameters: $\varepsilon_{\mathrm{thermal}}$, θ, $\Delta\mu_{\mathrm{contact}}$, and $\boldsymbol{A}_{\mathrm{lat},i} = -\bar{\bar{\boldsymbol{\varepsilon}}} \cdot \boldsymbol{K}_i$. They all have a major (order of magnitude) impact on the calculated conductivity. We included all of them in our study, and, to the best of our knowledge, it is the first time they have all been considered simultaneously.

Next, we present how the calculated conductivities are affected by excluding the following parameters: thermal strain in the contacts, gating in the contacts, and higher order strain effects. We also calculate the effect of reasonable uncertainties in v_F, β, and g_ε. All of these have a modest (10s of %) impact on the conductivity output. They were not included in the calculations to preserve the flexibility and ease of use of the model. We remark that these modest uncertainties will not misguide the experimental realization of the proposal, as they can be compensated for by adjusting the experimental parameters (θ, $\Delta\mu_{\mathrm{contact}}, V_{\mathrm{G}}, \varepsilon_{\mathrm{total}}$) within the studied range (see Fig. 4 of the main text).

Finally, we list the parameters whose uncertainties have minor (few %) effects on the conductivity. They include possible errors in the microfabricated dimensions L, W, and u, the presence of a realistic series resistance, R_{S}, between gold and graphene, a residual impurity density, n_{imp}, in the graphene channel, and uncertainties in the value of the Poisson ratio, ν, and anisotropy of the Fermi velocity. For the calculations below, unless specified otherwise, we use the same parameter-set as in the main text: $\beta = 2.5$, $g_\varepsilon = 3.0$ eV, $v_F = (3/2)a\gamma_0/\hbar = 8.8 \times 10^5$ m/s, $\nu = 0.165$, $L = 100$ nm, $W = 1000$ nm, $u = 900$ nm, $\Delta\mu_{\mathrm{contact}} = -0.12$ eV, $\theta = 30°$, $t_{\mathrm{vac}} = 50$ nm, $\varepsilon_{\mathrm{thermal}} = 2.6$ %, and $\varepsilon_{\mathrm{mech}} = 2.5$ %.

3.1 Major necessary corrections included in the transmission model

In Fig. S6 we show the effect of four parameters ($\varepsilon_{\mathrm{thermal}}$, θ, $\Delta\mu_{\mathrm{contact}}$, and $\boldsymbol{A}_{\mathrm{lat},i} = -\bar{\boldsymbol{\varepsilon}} \cdot \boldsymbol{K}_i$) which we have incorporated into our calculations to improve on previously idealized theoretical models. As can be seen in each panel, the exclusion of any of these parameters would cause major quantitative changes to the conductivity data, and misguide experiments. We therefore included realistic values for these terms in all of our calculations, as discussed in the main text.

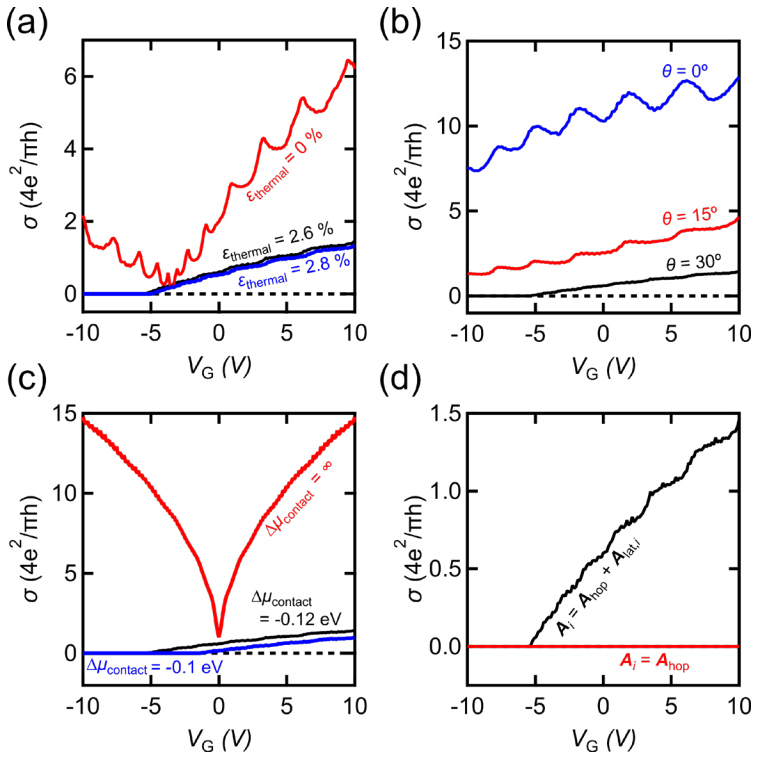

Figure S6. Corrections to transmission model with major impacts on $\sigma - V_{\mathrm{G}}$, when under a uniaxial strain of $\varepsilon_{\mathrm{thermal}} + \varepsilon_{\mathrm{mech}} = 2.6\ \% + 2.5\ \%$. (a) Effect thermal strain, with $\varepsilon_{\mathrm{thermal}} = 2.6\ \%$ (black), $\varepsilon_{\mathrm{thermal}} = 0\ \%$ (red), and $\varepsilon_{\mathrm{thermal}} = 2.8\ \%$ (blue). (b) Effect of the crystal orientation, with $\theta = 0°$ (black), $\theta = 15°$ (red), and $\theta = 0°$ (blue). (c) Effect of contact doping, with $\Delta\mu_{\mathrm{contact}} = -0.12$ (black), $\Delta\mu_{\mathrm{contact}} = \infty$ (red), $\Delta\mu_{\mathrm{contact}} = -0.1$ (blue). (d) Effect of including (black) or excluding (red) the lattice vector potential $\boldsymbol{A}_{i,\mathrm{lat}}$ from our calculations.

3.2 Modest uncertainties and corrections not included in our model – which can be compensated for by tuning experimental parameters

Figure S7, below, shows the impact of several other parameters on our $\sigma - V_G$ calculations. All of them have a modest (10s of %) effect on the calculated σ, and a much smaller effect on the $\sigma_{\mathrm{on/off}}$ ratio. We note that these corrections often have opposing signs, and would partially cancel each other. Moreover, the scale of the corrections can be compensated for with the experimentally controlled parameters, θ, $\Delta\mu_{\mathrm{contact}}$, V_{G}, and $\varepsilon_{\mathrm{total}}$ over the range presented in Fig. 4(c)-(d) of the main text. Therefore, in order to keep our applied theoretical model lightweight, intuitive and flexible, we did not include these

uncertainties or corrections. This will not undermine the ability of our model to properly guide the development of experiments.

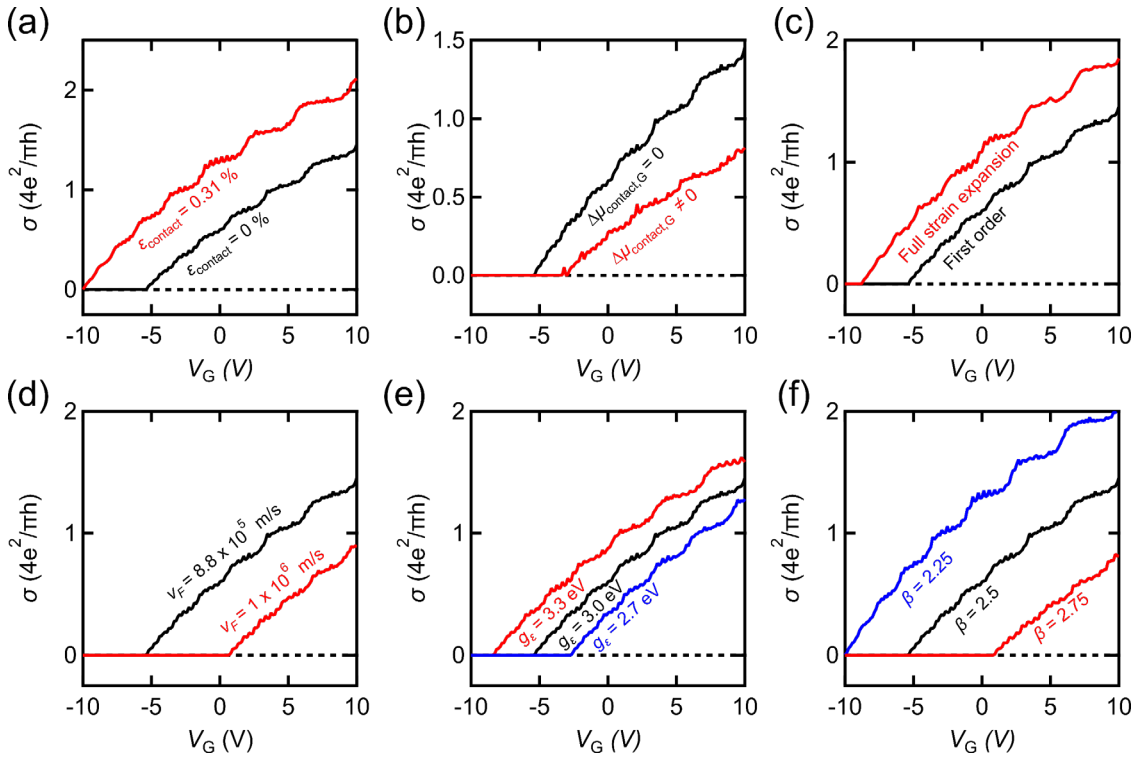

Figure S7. Parameter uncertainties with modest effects on $\sigma - V_G$, when under a uniaxial strain of $\varepsilon_{\text{thermal}} + \varepsilon_{\text{mech}} = 2.6\,\% + 2.5\,\%$. (a) Effect of excluding (black), or including (red) a strain in the contacts from gold contraction, $\varepsilon_{\text{contact}} = -0.31\,\%$. (b) Effect of excluding (black) or including (red) electrostatic gating of the Fermi energy in the contacts. (c) Effect of excluding (black) of including (red) higher order strain in the Hamiltonian. (d) Effect of uncertainty in the Fermi velocity, comparing $v_F = 8.8 \times 10^5$ m/s (black) and $v_F = 1 \times 10^6$ m/s (red). (e) Effect of varying the scalar potential prefactor, $g_\varepsilon = 3.0$ eV (black), 3.3 eV (red), and 2.7 eV (blue). (f) Effect of varying the electron Gruneisen parameter, $\beta = 2.5$ (black), 2.75 (red), and 2.25 (blue).

In Fig. S7(a), we show the effect of including strain in the graphene contacts. We expect any strain in the graphene contacts to arise from the contraction of the gold deposited on them. It should lead to a maximum, and isotropic, compressive strain of $\varepsilon_{\text{contact}} \approx -0.31\,\%$ at $T \sim 1$ K [S2]. The total effective vector potential governing the device would then be the difference in the positions of the Dirac points between the isotropically strained contacts and the uniaxially strained channel $\boldsymbol{A}_i \rightarrow \boldsymbol{K}_{D,i} - \boldsymbol{K}_{D,i,\text{contact}} = (\bar{\boldsymbol{\varepsilon}}_{\text{contact}} - \bar{\boldsymbol{\varepsilon}}) \cdot \boldsymbol{K}_i + \boldsymbol{A}_{\text{hop}}$, with

$$\bar{\boldsymbol{\varepsilon}}_{\text{contact}} = \begin{pmatrix} \varepsilon_{\text{contact}} & 0 \\ 0 & \varepsilon_{\text{contact}} \end{pmatrix}. \tag{S37}$$

There would be no hopping contribution from the vector potential in the isotropically strained contacts. In Fig. S7(b), we show the effect of including gating of the Fermi level in the graphene contacts. To calculate the Fermi energy in the back-gated graphene contacts, we follow Ref. [S13]:

$$\Delta\mu_{\mathrm{c,G}} = \mathrm{sgn}\left[\delta V_{\mathrm{G}} + \frac{\Delta\mu_{\mathrm{c}} C_{\mathrm{c}}}{e C_{\mathrm{G}}}\right]\left\{-\frac{C_{\mathrm{c}} + C_{\mathrm{G}}}{2}\zeta_F^2 + \sqrt{\left(\frac{C_{\mathrm{c}} + C_{\mathrm{G}}}{2}\zeta_F^2\right)^2 + \zeta_F^2 C_{\mathrm{c}}\left|\Delta\mu_{\mathrm{c}} + \frac{C_{\mathrm{G}}}{C_{\mathrm{c}}} e\delta V_{\mathrm{G}}\right|}\right\}, \quad \text{(S38)}$$

where we have replaced the subscript "contact" with "c" for brevity, $C_{\mathrm{c}} \approx 10^{-5}$ F/cm^2 is the capacitance between the metal and graphene sheet [S13], $\delta V_{\mathrm{G}} = V_{\mathrm{G}} - V_{\mathrm{D}}$, and $\zeta_F = \sqrt{\pi}\hbar v_F/e$ is the so-called Fermi electric flux. In Fig. S7(c), we show the effect of going beyond first order in strain when calculating the vector potentials. Using Eq. S16, we calculated the full-order strained graphene band structure, and numerically determined the positions of the Dirac points and vector potentials, $\boldsymbol{A}_i = \boldsymbol{K}_{D,i} - \boldsymbol{K}_i$. In Fig. S7(d)-(e)-(f), we show the effect of a $\sim$10 % uncertainty in the Fermi velocity, v_F, the scalar potential magnitude, g_ε, and the electron Grüneisen parameter, β.

3.3 Minor uncertainties and corrections not included in our model

Lastly, in Figure S8 we verify that several other minor uncertainties have no substantive impact of the quantitative predictions of the model.

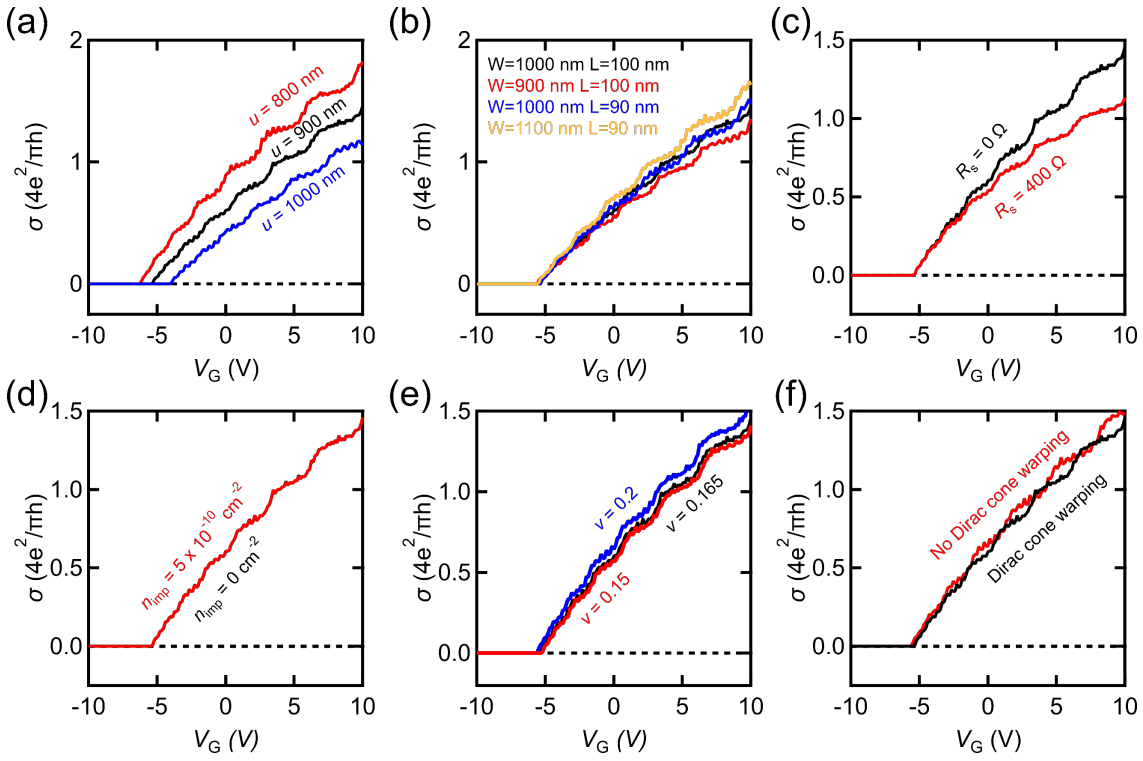

Figure S8. Parameter uncertainties with minor effects on $\sigma - V_{\mathrm{G}}$, when under a uniaxial strain of $\varepsilon_{\mathrm{thermal}} + \varepsilon_{\mathrm{mech}} = 2.6\,\% + 2.5\,\%$. (a) Effect of varying the undercut length $u = 900$ (black), 800nm (red), and $u = 1000$ nm (blue). (b) Effect of varying length and width of the graphene channel: $W = 1000$ nm, $L = 100$ nm (black), $W = 900$ nm, $L = 100$ nm (red), $W = 1000$ nm, $L = 90$ nm (blue), $W = 1100$ nm, $L = 90$ nm (gold). (c) Effect of excluding (black) or including (red) a series resistance $R_S = 400\ \Omega$. (d) Effect of excluding (black) or including (red) a channel impurity density $n_{\mathrm{imp}} = 5 \times 10^{10}$ cm^{-2}. (e) Effect of uncertainty in the Poisson ratio, $\nu = 0.165$ (black), $\nu = 0.15$ (red), $\nu = 0.2$ (blue). (f) Effect of including (black) or excluding (red) the strain-induced anisotropic Fermi velocity.

In Fig. S8(c) we show the effect of adding a series resistance R_S, arising from the gold-graphene injection. We plot conductivity ($\sigma \to L/W\,(\sigma^{-1}\,L/W + R_S)^{-1}$) adding a total series resistance of $R_S = 400\ \Omega$, due to the gold-graphene interface [S14]. We see that this has little effect on the low-conductivity data, as expected. Calculating the effect of R_S on the on/off ratio:

$$\sigma_{\mathrm{on/off}} = \frac{\frac{1}{\sigma_{\mathrm{off}}}\frac{L}{W} + R_S}{\frac{1}{\sigma_{\mathrm{on}}}\frac{L}{W} + R_S}. \tag{S39}$$

With $R_S = 400\ \Omega$, this corresponds to a reduction in $\sigma_{\mathrm{on/off}}$ of less than $20\ \%$.

In Fig. S8(d) we show the effect of including an impurity doping density of $n_{\mathrm{imp}} = 5 \times 10^{10}$ cm^{-2} [S15]. We include the impurity density using Eq. S40 below [S16]:

$$n_{\mathrm{total}} = \mathrm{sgn}(V_G - V_D)\sqrt{\left[\frac{(V_G - V_D)C_G}{e}\right]^2 + {n_{\mathrm{imp}}}^2}\,, \tag{S40}$$

and $\Delta\mu_G = \mathrm{sgn}(n_{\mathrm{total}})\sqrt{\pi|n_{\mathrm{total}}|}$. Due to the large scalar potential shift of the Dirac point, the impurity density has a negligible effect on the conductivity. In Fig. S8(e), we show the effect of varying the value of the Poisson ratio, $\nu = 0.15$ and $\nu = 0.2$. These curves show that small variances in the Poisson ratio have little effect on the conductivity data. In Fig. S8(f), we show the effect of excluding the Fermi velocity anisotropy, taking $v_{F,xx} = v_{F,yy} = v_F$ in Eq. S34. Excluding the warping of the Dirac cone does not significantly affect transport. We however did keep this last term in all calculations because it adds subtle qualitative changes in the FP resonances. Removing this correction would have no impact on our conclusions.

S4. Fano factor signatures of the GQST effect

The Fano factor is a measure of the shot noise in a system. It has a specific value for different transport regimes and can be used to study nonclassical dynamics. Here we remark that the Fano factor is also strain tunable. The Fano factor is readily calculated from the transmission [S6]:

$$F = \frac{\sum_\xi \sum_i^3 \sum_{n=0}^N T_{\xi,i,n}\,(1 - T_{\xi,i,n})}{\sum_\xi \sum_i^3 \sum_{n=0}^N T_{\xi,i,n}}. \tag{S41}$$

In Fig. S9(a), we show the conductivity as a function of gate and strain for device parameters $L/W = 100/1000$, $\theta = 15°$ $\Delta\mu_{\mathrm{contact}} = -0.12$ eV, and various strains. The Fano factor from the same dataset is shown in Fig. S9(b). It is well known that in the ballistic limit, the shot noise in graphene is sub-Poissonian, with the Fano factor reaching 1/3 at the Dirac point [S6]. However, as strain causes the conductivity to drop, the shot noise becomes Poissonian and the Fano factor approaches unity. Noise measurements could therefore be used as an additional way to confirm the GQST effect.

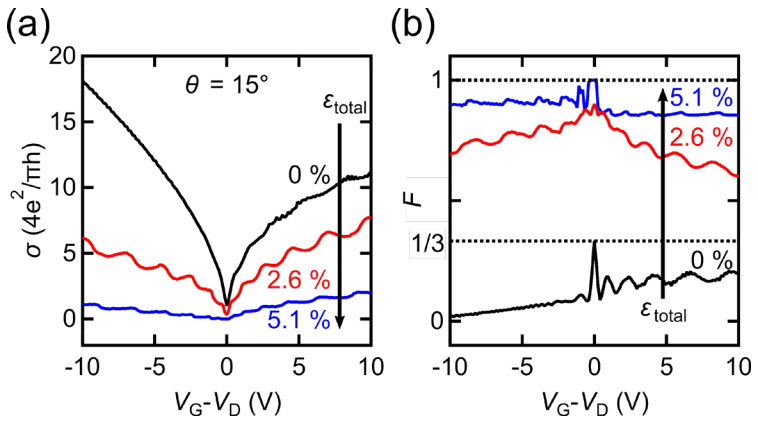

Figure S9. Fano factor signatures of the GQST effect. (a) $\sigma - (V_G - V_D)$ data for $\varepsilon_{total} = 0$, 2.6, and 5.1 % using device parameters $L/W = 100/1000$, $\theta = 15°$, $\Delta\mu_{contact} = -0.12$ eV. (b) Fano factor, *F*, vs. $(V_G - V_D)$ at various uniaxial strains.

Supplementary References

[S1] V. Singh, S. Sengupta, H.S. Solanki, R. Dhall, A. Allain, S. Dhara, P. Pant, and M. M. Deshmukh, Probing thermal expansion of graphene and modal dispersion at low-temperature using graphene nanoelectromechanical systems resonators, Nanotechnol. **21**, 165204 (2010).

[S2] F. C. Nix and D. MacNair, The thermal expansion of pure metals: copper, gold, aluminum, nickel, and iron, Phys. Rev. **60**, 597 (1941).

[S3] D. Yoon, Y. W. Son, and H. Cheong, Negative thermal expansion coefficient of graphene measured by Raman spectroscopy, Nano Lett. **11**, 3227 (2011).

[S4] J. O. Island, V. Tayari, A. C. McRae, and A. R. Champagne, Few-hundred GHz carbon nanotube nanoelectromechanical systems (NEMS), Nano Lett. **12**, 4564 (2012).

[S5] M. M. Fogler, F. Guinea, and M. I. Katsnelson, Pseudomagnetic fields and ballistic transport in a suspended graphene sheet, Phys. Rev. Lett. **101**, 226804 (2008).

[S6] J. Tworzydlo, B. Trauzettel, M. Titov, A. Rycerz, and C. W. Beenakker, Sub-Poissonian shot noise in graphene, Phys. Rev. Lett. **96**, 246802 (2006).

[S7] A. H. Castro Neto, F. Guinea, N. M. R. Peres, K. S. Novoselov, and A. K. Geim, The electronic properties of graphene, Rev. Mod. Phys. **81**, 109 (2009).

[S8] G. G. Naumis, S. Barraza-Lopez, M. Oliva-Leyva, and H. Terrones, Electronic and optical properties of strained graphene and other strained 2D materials: a review, Rep. Prog. Phys. **80**, 096501 (2017).

[S9] S. M. Choi, S. H. Jhi, and Y. W. Son, Effects of strain on electronic properties of graphene, Phys. Rev. B **81***,* 081407 (2010).

[S10] F. M. D. Pellegrino, G. G. N. Angilella, and R. Pucci, Transport properties of graphene across strain-induced nonuniform velocity profiles, Phys. Rev. B **84***,* 195404 (2011).

[S11] A. L. Kitt, V. M. Pereira, A. K. Swan, and B. B. Goldberg, Lattice-corrected strain-induced vector potentials in graphene, Phys. Rev. B **85***,* 115432 (2012).

[S12] V. M. Pereira, A. H. Castro Neto, and N. M. R. Peres, Tight-binding approach to uniaxial strain in graphene. Phys. Rev. B **80***,* 045401 (2009).

[S13] A. Laitinen, G. S. Paraoanu, M. Oksanen, M. F. Craciun, S. Russo, E. Sonin, and P. Hakonen, Contact doping, Klein tunneling, and asymmetry of shot noise in suspended graphene, Phys. Rev. B **93***,* 115413 (2016).

[S14] L. Anzi, A. Mansouri, P. Pedrinazzi, E. Guerriero, M. Fiocco, A. Pesquera, A. Centeno, A. Zurutuza, A. Benham, E. A. Carrion, E. Pop, and R. Sordan, Ultra-low contact resistance in graphene devices at the Dirac point, 2D Mater. **5**, 025014 (2018).

[S15] S. Yiğen, and A. R. Champagne, Wiedemann–Franz relation and thermal-transistor effect in suspended graphene, Nano Lett. **14**, 289 (2014).

[S16] V. E. Dorgan, M. H. Bae, and E. Pop, Mobility and saturation velocity in graphene on SiO_2, Appl. Phys. Lett. **97**, 082112 (2010).